Performance Analysis of MPC Controller for DFIG-WECS under Grid Voltage Unbalance by Considering Multi-Level Inverter based MSC and GSC

Mohd Arif, Kiran Kumar Jaladi

Electrical Engineering Department, National Institute of Technology Kurukshetra, Kurukshetra, Haryana, India

ARTICLEINFO	ABSTRACT
	This research work presents a model predictive current (MPC) controller for doubly fed induction generators (DFIG) and wind energy conversion systems (WECS) by employing a 5-level cascade H-bridge (CHB), an inverter-based machine side converter (MSC), and a grid side converter (GSC). The proposed MPC system is used to effectively control MSC and GSC operation under unbalanced grid voltage conditions. Here, 5-level CHB is employed in MSC and GSC to reduce harmonics and improve both converters' performance. In this paper, the proposed MPC is implemented and compared with the conventional PI controller. Under unbalanced grid voltage conditions, the obtained proposed MPC results outperform a conventional PI controller. The entire proposed MPC controller for DFIG-WECS employing 5-Level CHB is implemented and tested using MATLAB/SIMULINK 2018a software. **Keywords** : DFIG, MPC, MLI, PI, WECS, GSC, MSC, CHB

I.   INTRODUCTION

The fastest-growing renewable energy technology is wind energy generation, according to reports. In particular when there are anomalous grid voltage conditions, the growing wind energy penetration level may have a substantial effect on the grid. Therefore, to sustain reliability during and after a short-term fault, wind turbines (WTs) must engage in steady-state grid voltage support and remain connected to the grid, according to the power grid connection codes in most nations [1]. The latter criterion calls for WTs to send reactive currents to the grid in accordance with the grid rules, such as those of the US FERC [3] and German E.ON [2].

The doubly fed induction generator (DFIG) is one of the most widely used wind turbine concepts because of its high energy efficiency, reduced mechanical stress on the wind turbine, separately controllable active and reactive power, and relatively low power rating of the connected converter [4]. However, because the stator is connected directly to the grid, the DFIG is extremely susceptible to grid faults [5]. In order to satisfy the LVRT requirements of DFIGs during voltage sags, two key issues must be resolved.

First, the rotor circuit of the DFIG experiences an overcurrent that could harm the rotor side converter (RSC), and second, the dc-link experiences an overvoltage. Both of these are caused by the extra energy that is unable to enter the grid due to faults [6]. As a result, additional precautions must be taken to protect them from various voltage sag conditions.

Numerous experiments have been conducted in an effort to increase the LVRT capacity of DFIG WT. When overloads are discovered, protective tools like crowbars are frequently employed to bypass the rotor side converter among the options [7-9]. When the crowbar is activated, however, the machine's controllability is gone, and DFIG turns into a standard induction machine. In this instance, the generator consumes a significant amount of reactive power from the grid rather than supporting it, which is detrimental to the system's ability to recover. There are also suggested approaches for DFIG fault ride through that include the use of additional hardware, such as a series dynamic resistance in the rotor and stator [10] or a series line side converter (LSC) topology as suggested in [12]. Recently, it was also looked into how to improve the LVRT capability of the DFIG during grid failures by using a dynamic voltage restorer and a superconducting fault-current limiter-magnetic energy storage system, respectively, in [13,14]. However, these methods call for adding more hardware to the DFIG WT system, which will raise costs and reduce system dependability.

In order to improve the grid voltage unbalance capability of the DFIG WT, this paper expands the MPC presented and suggests an improved control strategy for both the MSC and GSC. This is done by simultaneously suppressing the surge and harmonics in the rotor current as well as the fluctuation of the DC-link voltage

The following describes how the paper is structured: The proposed system description is presented in Section 2. Proposed method is presented in Section 3, simulation results and discussion is presented in Section 4. Conclusion is presented in Section 5.

II. SYSTEM DESCRIPTION

Modelling of the DFIG Wind Turbine

Figure 1 depicts the schematic layout of a DFIG WT system that is grid-connected. The back-to-back voltage source converter with a common dc-link, the induction generator, the drive train, the control system, and the wind turbine are all parts of the DFIG WT system that are connected to the grid via a transformer. In order to decrease the harmonics the back-to-back converters create, a line filter connects the RSC and GSC to the grid. While the GSC controls the common dc-link voltage, the RSC's primary duty is to regulate the active and reactive power output of the DFIG stator.
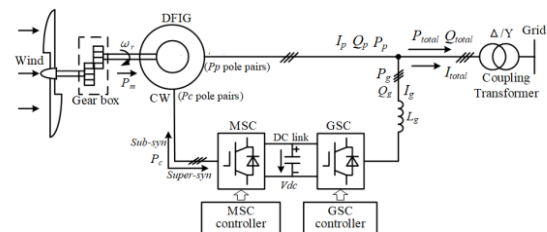

Figure 1. Schematic diagram of a grid-connected DFIG WT system.

To secure the RSC from over-current, a completely bridge rectifier, a resistor, and a fully controlled switch are used in an active crowbar circuit, as depicted in Figure 1. To protect the RSC and GSC against dc bus overvoltage, a dc chopper circuit with a 0.5 per unit (pu) resistor is also in place across the dc bus.

i)Wind Turbine Aerodynamics Model

The dynamics of the mechanical component of the turbine will be disregarded due to the small duration of voltage disturbances, and the mechanical torque generated by the wind is assumed to be constant.

ii)Drive Train Model

The two-mass model of the drive train that is frequently used to depict dynamic stability of the DFIG WT is given by the following to analyse the effects of voltage dips on the mechanical system:

$$\frac{d}{dt}\begin{bmatrix}\Delta\omega_t\\\Delta\omega_r\\T_g\end{bmatrix}=\begin{bmatrix}\frac{-D_t-D_{tg}}{2H_t}&\frac{D_{tg}}{2H_t}&\frac{-1}{2H_t}\\\frac{D_{tg}}{2H_g}&\frac{-D_g-D_{tg}}{2H_g}&\frac{1}{2H_g}\\K_{tg}\omega_e&-K_{tg}\omega_e&0\end{bmatrix}\begin{bmatrix}\Delta\omega_t\\\Delta\omega_r\\T_g\end{bmatrix}+\begin{bmatrix}\frac{T_m}{2H_t}\\\frac{-T_e}{2H_g}\\0\end{bmatrix}$$

1

Where the turbine, generator rotor, and nominal rotating speed, respectively, are represented by t, r, and 0; Tm and Te stand for the mechanical (here assumed constant) and electrical (here assumed electromagnetic) torques of the generator, respectively;

Tg is a model's internal torque; Ht and Hg are the generator's and turbine's respective inertia constants; Dt and Dg are the two masses' respective mechanical damping coefficients; Dtg is the shaft's damping coefficient; and Ktg is the shaft stiffness. The damping coefficient and the shaft stiffness between the turbine and the generator, which are given by Dt = Dg = Dtg = 0, Ktg = 0, and Ht = Hg = H, respectively, will not be considered in this study. It is transformed into the lumped-mass model of the drive train, and the formula is as follows:

$$T_e = 2H\omega_r + T_m$$

2

iii)Induction Generator Model

In a d-q reference frame rotating at any speed, the voltage equations of the stator and rotor circuits of the induction generator can be stated.

$$\begin{cases}u_{ds}=r_s i_{ds}+p\psi_{ds}-\omega\psi_{qs}\\u_{qs}=r_s i_{qs}+p\psi_{qs}+\omega\psi_{ds}\\u_{dr}=r_r i_{dr}+p\psi_{dr}-(\omega-\omega_r)\psi_{qr}\\u_{qr}=r_r i_{qr}+p\psi_{qr}+(\omega-\omega_r)\psi_{dr}\end{cases}$$

3

$$\begin{cases}\psi_{ds}=L_s i_{ds}+L_m i_{dr}\\\psi_{qs}=L_s i_{qs}+L_m i_{qr}\\\psi_{dr}=L_m i_{ds}+L_r i_{dr}\\\psi_{qr}=L_m i_{qs}+L_r i_{qr}\end{cases}$$

4

A.Where the vectors of flux, voltage, and current are represented by, u, and I respectively. The stator and rotor quantities are indicated by the subscripts s and r, respectively. The letters d and q stand for the d- and q-axis components, respectively. The stator and rotor

angular frequencies are denoted by s and r, respectively. The d-q reference frame's speed is. Lm is the mutual inductance, while Ls, Lr, and Lm, respectively, and are the stator and rotor self-inductances. The stator and rotor resistances, rs and rr, respectively, are also included. The differential operator is called p.

A.CONTROL OBJECTIVES AND CALCULATION OF CURRENT REFERENCE VALUES FOR MSC AND GSC

1) MSC (DFIG)

In essence, wind turbines must stay connected to the electrical grid in the event of a grid voltage unbalance, per grid code requirements. However, considerable oscillations in the electromagnetic torque, PW active and reactive power exist and are exceedingly dangerous, as discussed in Section III. Because it may harm the shaft, gearbox, and other mechanical parts and cause the wind turbines to be disconnected from the power grid, electromagnetic torque oscillations among them in particular have a major negative impact on the safe and stable operation of the wind turbine system. Therefore, electromagnetic torque oscillation suppression is necessary for the DFIG system to operate steadily. Furthermore, the grid code mandates that during grid voltage unbalance, the wind turbines must be able to independently control active and reactive power. Based on the foregoing analysis, the control targets of the MSC are established in this study to achieve decoupling control for the average PW active power Pp0 and reactive power Qp0 while also eliminating the DFIG torque oscillations.

The four CW current components for MSC, I + cd+, I + cq+, I cd, and I cq, can also be adjusted to fulfil the aforementioned control objectives The average PW active power Pp0 and reactive power Qp0 are often controlled by I + cd+ and I + cq+, while I cd+ and cd+ are utilised to eliminate electromagnetic torque oscillations. Furthermore, it is possible to achieve V + pd+ = V + gd+ = V + g and V + gd+ = V + gq+ = 0 utilising the grid voltage orientation (GVO) technique

for MSC (DFIG), disregarding the yields of the PW flux transient and PW resistance Rp

$$V_{pdq+}^+ = V_{pd+}^+ + jV_{pq+}^+ = V_{pd+}^+ \approx j\omega_p \psi_{pdq+}^+$$
$$V_{pdq-}^- = V_{pd-}^- + jV_{pq-}^- \approx -j\omega_p \psi_{pdq-}^-$$

5

Thus, the necessary control reference values of the MSC (CW) currents may be simply determined by using substituting Tems2 = 0 and Temc2 = 0 into the references of the average PW active power P p0 and reactive power Q p0 respectively.

$$\begin{cases} I_{cd+}^{+*} = \dfrac{2L_M V_{pd+}^+ P_{p0}^*}{3L_{cr}\left(V_{pd+}^{+2} + V_{pd-}^{-2} + V_{pq-}^{-2}\right)} \\ I_{cq+}^{+*} = -\dfrac{2L_M V_{pd+}^+ Q_{p0}^*}{3L_{cr}\left(V_{pd+}^{+2} - V_{pd-}^{-2} - V_{pq-}^{-2}\right)} - \dfrac{L_r V_{pd+}^+}{L_{pr} L_{cr} \omega_p} \\ I_{cd-}^{-*} = \dfrac{V_{pd-}^-}{V_{pd+}^+}I_{cd+}^{+*} + \dfrac{V_{pq-}^-}{V_{pd+}^+}I_{cq+}^{+*} \\ I_{cq-}^{-*} = \dfrac{V_{pq-}^-}{V_{pd+}^+}I_{cd+}^{+*} - \dfrac{V_{pd-}^-}{V_{pd+}^+}I_{cq+}^{+*} \end{cases}$$

6

Additionally, the necessary control reference values for the MSC(CW) positive and negative sequence currents can be calculated by replacing Qps2 = 0, Qpc2 = 0, P p0, and Q p0. (6).

This suggests that if (6) is met, oscillations in the DFIG electromagnetic torque and PW reactive power can be reduced concurrently.

2) GSC

Studies that have already been done on grid voltage unbalance have only addressed at how to control the MSC side of the BDFIG wind turbine system. However, in order to ensure the secure and reliable functioning of the power system, wind turbines must also be able to eliminate imbalanced total output current and oscillations of the total output active or reactive power at the point of common connection (PCC). However, these control objectives cannot be attained only through the control of MSC due to the constrained control variables of MSC. In order to further improve the ability of the DFIG wind turbine system to endure grid voltage unbalance, the GSC current components, i.e., I + gd+, I + gq+, I + gd+ and I + gq+, are utilised in this research, as shown in Fig. 1 and specified in (35) and (36). Based on the study

above, GSC are managed in concert with MSC to meet three chosen control objectives: Objective I: removing the imbalance in the total output current Objective II is to stop the power grid's total output active power from oscillating. Eliminating fluctuations in the total output reactive power into the power system is Objective III.

$$I_{p\alpha\beta-}^- + I_{g\alpha\beta-}^- = I_{pdq-}^- e^{-j\omega_p t} + I_{gdq-}^- e^{-j\omega_p t} = 0$$

7

Therefore, in accordance with (7), the required control reference values for the positive and negative sequence of GSC currents can be directly calculated as follows by substituting the references of the average GSC active power P g0 and reactive power Q g0 into (5) and accounting for grid voltage orientation for GSC, i.e., V + gd+ = V + g+, V + gq+ = 0.

$$\begin{cases} I_{gd+}^{+*} = \dfrac{-2P_{g0}^*}{3V_{gd+}^+} + \dfrac{V_{gd-}^-}{V_{gd+}^+}I_{pd-}^- + \dfrac{V_{gq-}^-}{V_{gd+}^+}I_{pq-}^- \\ I_{gq+}^{+*} = \dfrac{2Q_{g0}^*}{3V_{gd+}^+} - \dfrac{V_{gq-}^-}{V_{gd+}^+}I_{pd-}^- + \dfrac{V_{gd-}^-}{V_{gd+}^+}I_{pq-}^- \\ I_{gd-}^{-*} = -I_{pd-}^- \\ I_{gq-}^{-*} = -I_{pq-}^- \end{cases}$$

8

The total active power for Objective II, as seen in Fig. 1, is the product of the active power outputs from the DFIG PW and the GSC, or Total=Pp+Pg.

$$P_{total} = (P_{p0} + P_{g0}) + (P_{ps2} + P_{gs2})\sin 2\omega_p t \\ + (P_{pc2} + P_{gc2})\cos 2\omega_p t$$

9

Accordingly, based on (9), the GSC active power oscillations must be managed to fulfil with in order to stop the oscillations of the total active power.

$$\begin{cases} P_{gs2} + P_{ps2} = 0 \\ P_{gc2} + P_{pc2} = 0 \end{cases}$$

10

By directly calculating the required control reference values for the positive and negative sequence of GSC currents using (10) as well as the references of the average GSC active power P g0 and reactive power Q g0 and taking into account grid voltage orientation, i.e., V + gd+ = V + g+, V + gq+ = 0,

$$\begin{cases} I_{gd+}^{+*} = \dfrac{-2\left(V_{gd+}^{+}P_{g0}^{*} + V_{gd-}^{-}P_{pc2} + V_{gq-}^{-}P_{ps2}\right)}{3\left(V_{gd+}^{+2} - V_{gd-}^{-2} - V_{gq-}^{-2}\right)} \\[3mm] I_{gq+}^{+*} = \dfrac{2\left(V_{gd+}^{+}Q_{g0}^{*} - V_{gd-}^{-}P_{ps2} + V_{gq-}^{-}P_{pc2}\right)}{3\left(V_{gd+}^{+2} + V_{gd-}^{-2} + V_{gq-}^{-2}\right)} \\[3mm] I_{gd-}^{-*} = \dfrac{2P_{pc2}}{3V_{gd+}^{+}} - \dfrac{V_{gd-}^{-}}{V_{gd+}^{+}}I_{gd+}^{+*} - \dfrac{V_{gq-}^{-}}{V_{gd+}^{+}}I_{gq+}^{+*} \\[3mm] I_{gq-}^{-*} = \dfrac{2P_{ps2}}{3V_{gd+}^{+}} - \dfrac{V_{gq-}^{-}}{V_{gd+}^{+}}I_{gd+}^{+*} + \dfrac{V_{gd-}^{-}}{V_{gd+}^{+}}I_{gq+}^{+*} \end{cases} \quad \textbf{11}$$

Similar to Objective II, Q total = Qp + Qg according to Fig. 1. Additionally, Qps2 = 0, Qpc2 = 0 is used to control MSC in order to completely prevent oscillations in both DFIG electromagnetic torque and PW reactive power. Therefore, Qgs2 = 0 and Qgc2 = 0 must be satisfied in order to stop oscillations in the total output reactive power.
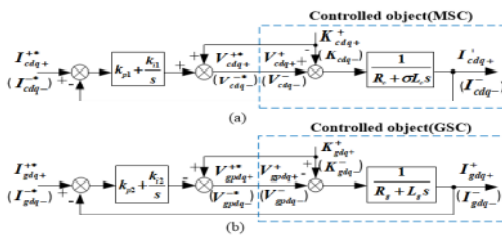
FIGURE 2. Current controllers in (dq) + and (dq) − reference frame. (a)MSC current controller.

(b) GSC current controller.

The required references of GSC currents can be calculated as

$$\begin{cases} I_{gd+}^{+*} = \dfrac{-2V_{gd+}^{+} + P_{g0}^{*}}{3\left(V_{gd+}^{+2} + V_{gd-}^{-2} + V_{gq-}^{-2}\right)} \\[3mm] I_{gq+}^{+*} = \dfrac{2V_{gd+}^{+} + Q_{g0}^{*}}{3\left(V_{gd+}^{+2} - V_{gd-}^{-2} - V_{gq-}^{-2}\right)} \\[3mm] I_{gd-}^{-*} = \dfrac{V_{gd-}^{-}}{V_{gd+}^{+}}I_{gd+}^{+*} + \dfrac{V_{gq-}^{-}}{V_{gd+}^{+}}I_{gq+}^{+*} \\[3mm] I_{gq}^{-*} = \dfrac{V_{gq-}^{-}}{V_{gd+}^{+}}I_{gd+}^{+*} - \dfrac{V_{gd-}^{-}}{V_{gd+}^{+}}I_{gq+}^{+*} \end{cases} \quad \textbf{12}$$

B. CURRENT CONTROLLER DESIGN

Both the MSC and GSC must be managed in order for their positive and negative sequence currents to follow the suggested coordinated control reference values in order to meet the proposed coordinated control objectives. The current control design would employ a straightforward single loop controller made up of a positive sequence current controller in the positive synchronous reference frame and a negative sequence current controller in the negative synchronous reference frame.

1) MSC (DFIG) existing controller First, it is possible to determine I + cd+, I + cq+, I cd+, and I cq+ based on P p0, Q p0, and (7). The current controller can then be developed as shown in (14) and (20) by utilising decoupling control and feedback control.

$$V_{cdq+}^{+*} = k_{p1}(I_{cdq+}^{+*} - I_{cdq+}^{+}) + k_{i1}\int (I_{cdq+}^{+*} - I_{cdq+}^{+}) + K_{cdq+}^{+} \quad \textbf{13}$$

$$V_{cdq-}^{-*} = k_{p1}(I_{cdq-}^{-*} - I_{cdq-}^{-}) + k_{i1}\int (I_{cdq-}^{-*} - I_{cdq-}^{-}) + K_{cdq-}^{-} \quad \textbf{14}$$

where K + cdq+ and K cdq+ are the terms used for feedforward control and expressed, where PW flux can be further eliminated by using GVO approach and where V + cdq+ and V cdq refer to the CW control voltages from the positive sequence current controller and negative sequence current controller, respectively (5). The suggested MSC current controller's control diagram may be seen in Fig. 6 and is based on (13) and (14). (A). the first step is to construct a single current closed-loop controller without considering CW flux, PW flux, or RW current estimates. As a result, it is significantly more clear and practical and has superior parameter robustness. The cross-coupling terms and disturbances designated as K + cdq+ and K cdq are all derived and employed for decoupling control in current loops, respectively. Decoupling control for the average PW active and reactive power can also be obtained, and as a result, complete decoupling control for the d-axis and q-axis currents can be realised. The efficiency of the suggested current controller has thus been theoretically confirmed based on the analysis above. The outputs from the positive and negative sequence current controllers are combined to provide the overall MSC (CW) control voltage. In the (cc) reference frame, it can be presented as shown in Fig. 4 and (13).

$$V_{c\alpha\beta}^{*} = V_{cdq+}^{+*}e^{j[\theta_p - (p_p + p_c)\theta_r]} + V_{cdq-}^{-*}e^{-j[\theta_p - (p_p + p_c)\theta_r]} \quad \textbf{15}$$

The GSC current controller I + gd+, I + gq+, I gd and I gq can first be found according to P g0, Q g0, and (8), (11) or (12). In a similar manner, the GSC current controllers in the (dgqg) + and (dgqg) employing decoupling control and feedback control.

$$V_{gpdq+}^{+*} = -\left[k_{p2}(I_{gdq+}^{+*} - I_{gdq+}^{+}) + k_{i2}\int (I_{gdq+}^{+*} - I_{gdq+}^{+})\right]$$

$$+ K_{gdq+}^+ \qquad 16$$

$$V_{gpdq-}^{-*} = -\left[k_{p2}(I_{gdq-}^{-*} - I_{gdq-}^-) + k_{i2} \int (I_{gdq-}^{-*} - I_{gdq-}^-) \right]$$

$$+ K_{gdq-}^- \qquad 17$$

where kp2 and ki2 stand for the proportional and integral gains of the current controller, respectively, and V + gdq+ and V gdq for the GSC control voltages from the positive sequence current controller in (dgqg) + reference frame and the negative sequence current controller in (dgqg) reference frame. K + gdq+ and K gdq stand for all cross-coupling terms and disturbances used for feed

$$\begin{cases} K_{gdq+}^+ = V_{gdq+}^+ + j\omega_p L_g I_{gdq+}^+ \\ K_{gdq-}^- = V_{gdq-}^- - j\omega_p L_g I_{gdq-}^- \end{cases} \qquad 18$$

Fig. 2 depicts the control diagram of the GSC current controller in accordance with (16) and (17). Similar to this, the combined outputs from the positive and negative sequence current controllers make up the total GSC control voltage. In (gg) reference frame, it can be supplied as shown in Fig.

$$V_{gp\alpha\beta}^* = V_{gpdq+}^{+*} e^{j\theta_g} + V_{gpdq-}^{-*} e^{-j\theta_g} \qquad 19$$

From the above design of MSC and GSC controllers, to effectively control the positive and negative sequence
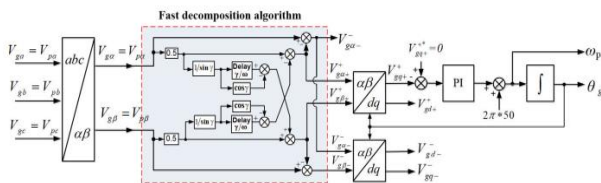
FIGURE 3. Enhanced PLL for MSC and GSC based on fast decomposition algorithm

The MSC and GSC, which are parts of the CW and GSC currents, must produce both positive and negative sequence control voltages in the presence of grid voltage unbalance. This might improve the MSC and GSC ratings for those underbalanced grid voltage situations. In general, larger MSC and GSC ratings are needed the higher the grid voltage unbalanced. A more thorough analysis of the back-to-back converter

rating under grid voltage unbalance will be examined into later due to space constraints.

C. FAST SEQUENCE DECOMPOSITION ALGORITHM AND ENHANCED PLL

The voltages, flux, and currents must be divided into both positive and negative sequence components for the proposed control. The process of sequence decomposition adds significant amplitude and phase errors to the signals, which has a severe impact on the control characteristics and stability of the wind turbine system. Normally, notch filters are employed to extract positive and negative sequence components. Instead of employing notch filters in this study to address these issues, a fast sequence decomposition approach from further boost the effectiveness of the entire control system. Fig. 3 depicts a quick decomposition algorithm. In Figure 3, 1t = / denotes the moment at which the positive and negative sequence components are divided into their component frequencies. Unlike notch filters, this quick sequence decomposition algorithm only utilises the sample data at two points on the three-phase variable curves to determine the positive and negative sequence components. In the extreme example, the sequence component can be determined using the present value and its derivative if the time 1t between these two points is relatively short. As a result, this approach responds significantly faster than filters and has no amplitude mistakes. For instance, if the sampling frequency of the wind turbine system is 2.55 kHz and the frequency of the power grid is 50 Hz, the decomposition time is 1t = 392 us, and if the delayed time is equal to the sampling period, the decomposition time is 1t = 0.039. Enhance PLLs for both MSC and GSC are created based on the quick sequence decomposition approach; these are also shown in Fig.3.

III. PROPOSED METHOD
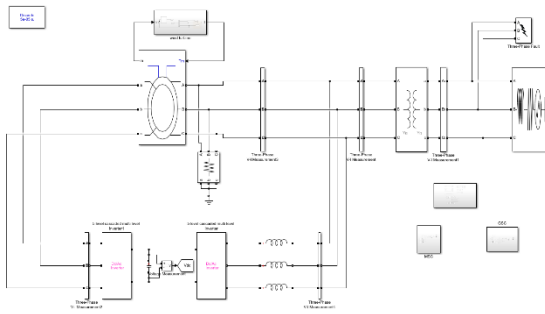
Fig 4 simulation diagram of proposed method

To control GSC and MSC in this study, a MPC controller is proposed instead of a PI controller. Here, GSC and RSC employed a 5-level CHB inverter in place of a 2-level inverter.

MPC Control for DFIG

The inner loop controller controls the current and outputs the voltage on the two-phase rotating coordinate axis after receiving a reference current from the MPC. The voltage on the two-phase stationary coordinate axis is measured after the Park inverse transform, and the SVPWM module is used to produce the PWM signal. The PWM signal is then utilised to drive the inverter, which creates a three-phase sinusoidal alternating current with adjustable amplitude and frequency that powers the DFIG. The Park transform module's output of the q-axis current serves as feedback for the current-loop MPC controller, and the feedback module's output of speed is transmitted back to the speed-loop MPC controller. In this manner the double closed-loop MPC system is realized for DFIG. The design of MPC controller includes four parts:
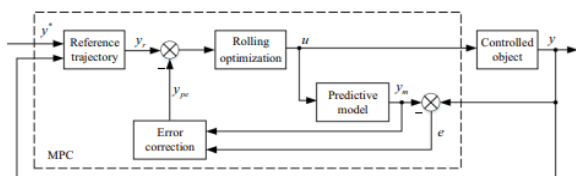
Fig. 5 The structure of predictive control

Reference trajectory, rolling optimization, and error correction comprise a predictive model. The MPC controller is depicted as a dotted box in Fig. 2, which illustrates the predictive control structure. The

following lists the precise design procedures for the q-axis current-loop MPC and the speed-loop MPC. Different state space models exist for the speed-loop MPC and the q-axis current-loop MPC. The error correction, reference trajectory, and optimization criterion modules' design approaches, however, are applicable to both MPCs.

The following are the primary benefits of the suggested MPC strategy: 1) The double closed-loop MPC technique that has been proposed has good speed tracking performance, no overshoot, and good load disturbance resistance. Therefore, the offered technique performs more dynamically. 2) The proposed MPC approach has a superior stator current waveform than the PI controller. The MPC technique reduces the current harmonics, which minimizes the damage to the motor. Therefore, the suggested technique offers improved steady-state performance.

Multi-level inverters

For grid connectivity, many multilayer topologies are employed. There are three main types of multilevel converter structures: cascaded H-bridge inverters (CHBI), flying capacitors (FC), and neutral point clamped (NPC or diode clamped). The multilevel CHBI has many advantages over the latter two, including: A reduced harmonic content in the output voltage is achieved for a given switching frequency; A lower requirement for switch devices under the same switching frequency and level number. Because each cell has the same structure and does not require additional clamping diodes (as in the case of diode clamped topology) or voltage balancing capacitors (as in the case of capacitor clamped topology), modularized circuit layout and packaging are achievable.

Three-Phase CHB Inverter Topologies

The conventional three-phase, five-level CHB inverter is shown in Figure 1. A five-level output voltage was produced using two H-bridge circuits in each phase. The isolated DC voltage source was attached to each H-bridge module. The H-bridge leg's upper and lower switches cannot be turned on at the

same time in a standard CHB inverter. In the H-bridge circuit, the dead-time between the upper and lower switches should be used to prevent the ST phenomena.
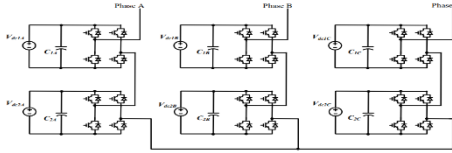
Figure 6. Construction of three-phase 5 level cascaded H-bridge (CHB) inverter topology.
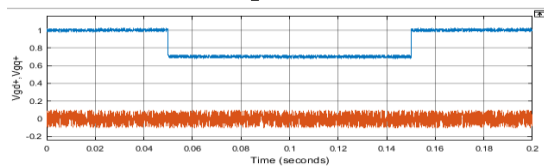
IV. RESULTS AND DISCUSSION
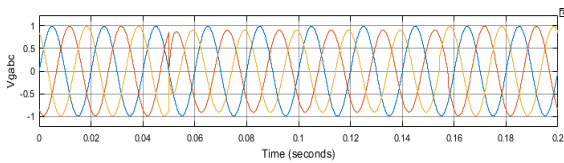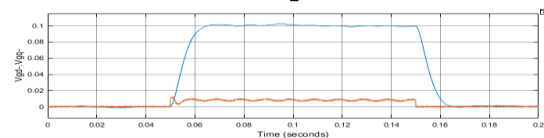

7(a) Grid voltage Vgabc (p.u.).
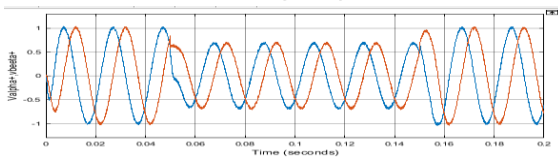
7(b) Positive sequence component in reference frame (p.u.)
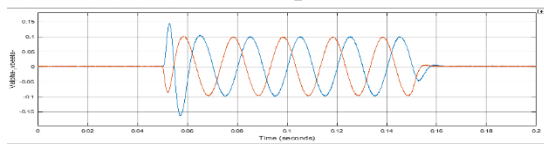
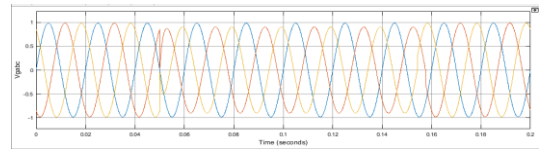7(c) Negative sequence component in reference frame (p.u.).
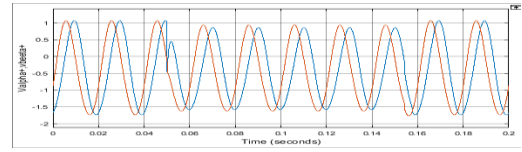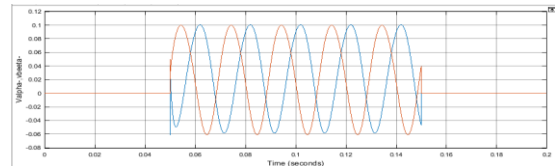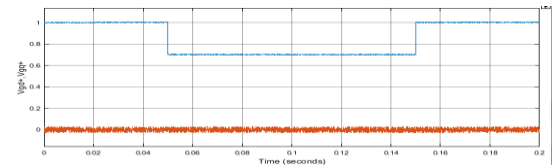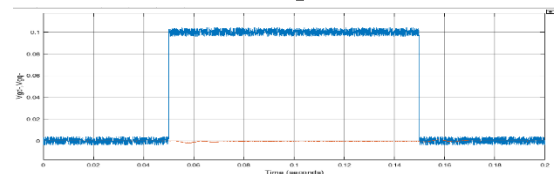

7d) Positive sequence component in (dq) C reference frame (p.u.).

7(e) Negative sequence component in (dq) reference frame (p.u.).

FIG 7 Fast decomposition method with conventional PI controller

8(a) Grid voltage Vgabc (p.u.).

8(b) Positive sequence component in reference frame (p.u.)

8(c) Negative sequence component in reference frame (p.u.).

8d) Positive sequence component in (dq) C reference frame (p.u.).

8(e) Negative sequence component in (dq) reference frame (p.u.).

FIGURE 8. Fast decomposition method with MPC-5-level CHB Sequence decomposition results of grid voltage with notch filter and fast decomposition algorithm. (B) Fast sequence decomposition algorithm

Using a notch filter and quick decomposition algorithm, the grid voltage decomposition results are shown in Fig. 7&8. Fig. 7&8 (a) depicts the grid voltage waveform, in which a 0.1 p.u. negative sequence component and a 0.2 p.u. sag with its amplitude appear at 0.05 s and 0.15 s, respectively. Figures 7&8 (b), 7&8 (c), 7&8 (d), and 7&8 (e) show that the rapid decomposition algorithm significantly speeds up the decomposition process compared to the notch filter (around 50 ms). Additionally, as observed from Fig. 7&8, fast decomposition technique has

significantly superior dynamic properties throughout the decomposition process than notch filter and does not have amplitude problems.
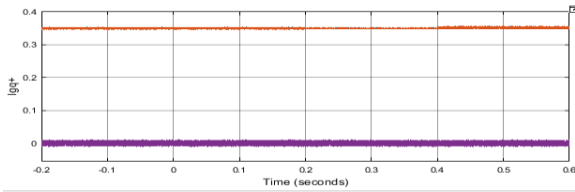
9(a) Total output current (p.u.).
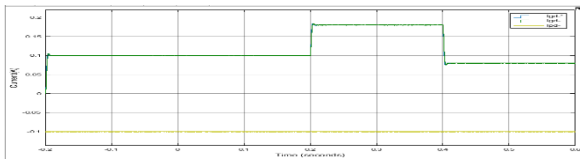
9(b) GSC d- axis and PW q- axis currents (p.u.).
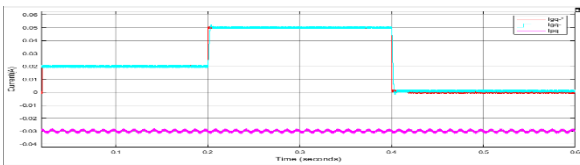
9(c) GSC q- axis and PW d-axis currents (p.u.). (d) GSC DC axis and qC axis currents (p.u.).
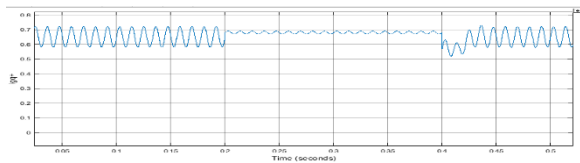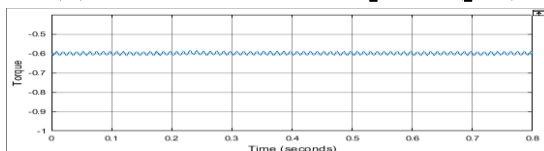

9 (e) Total output active power (p.u.).
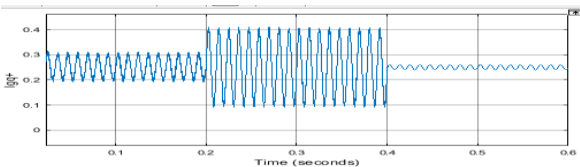
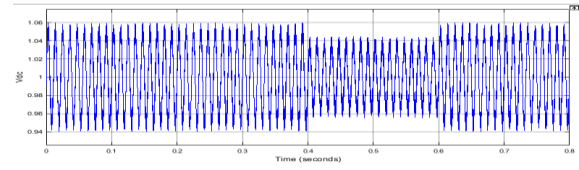
9 (f) PW and GSC active power (p.u.).
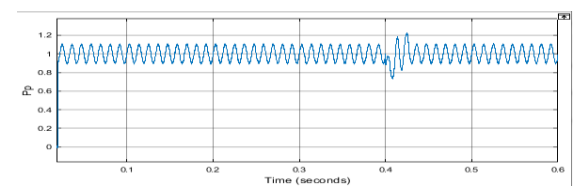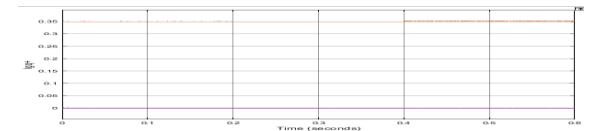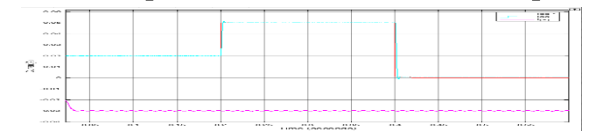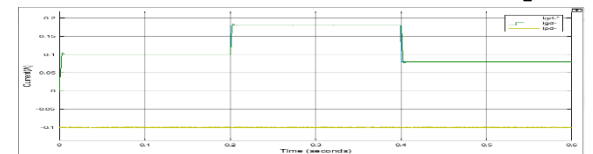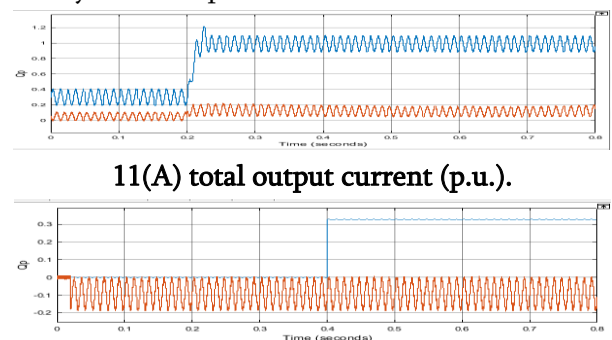

9 (g) Total output reactive power (p.u.).
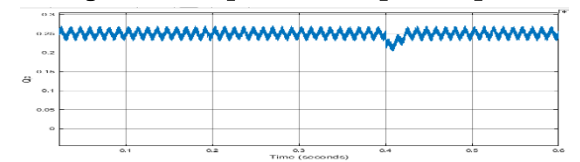
9 (h) PW and GSC reactive power (p.u.).

9 (i) Electromagnetic torque (p.u.).

9 (j) DC link voltage (p.u.).
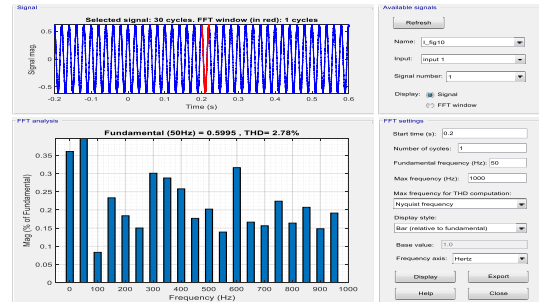
FIGURE 9. Waveforms with elimination of torque oscillations and three selectable control objectives under 10% grid voltage unbalance (! r D 0:7 p.u., "D 10%)
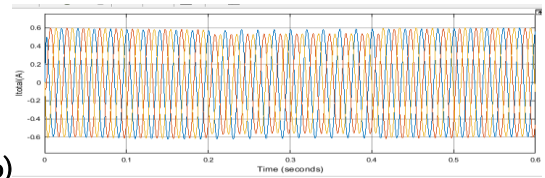
10(a) Total output current (p.u.).
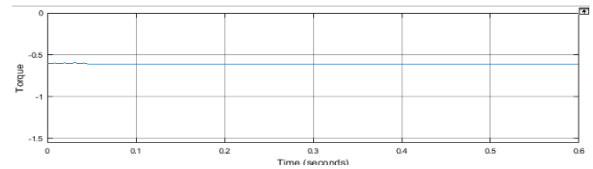
10(b) GSC d- axis and PW q- axis currents (p.u.).

10(c) GSC q- axis and PW d-axis currents (p.u.).

10(d) GSC DC axis and QC axis currents (p.u.).

10(e)Total output active power (p.u.).

10(f) PW and GSC active power (p.u.).

10(g) Total output reactive power (p.u.).

10(h) PW and GSC reactive power (p.u.).

10(i) Electromagnetic torque (p.u.).
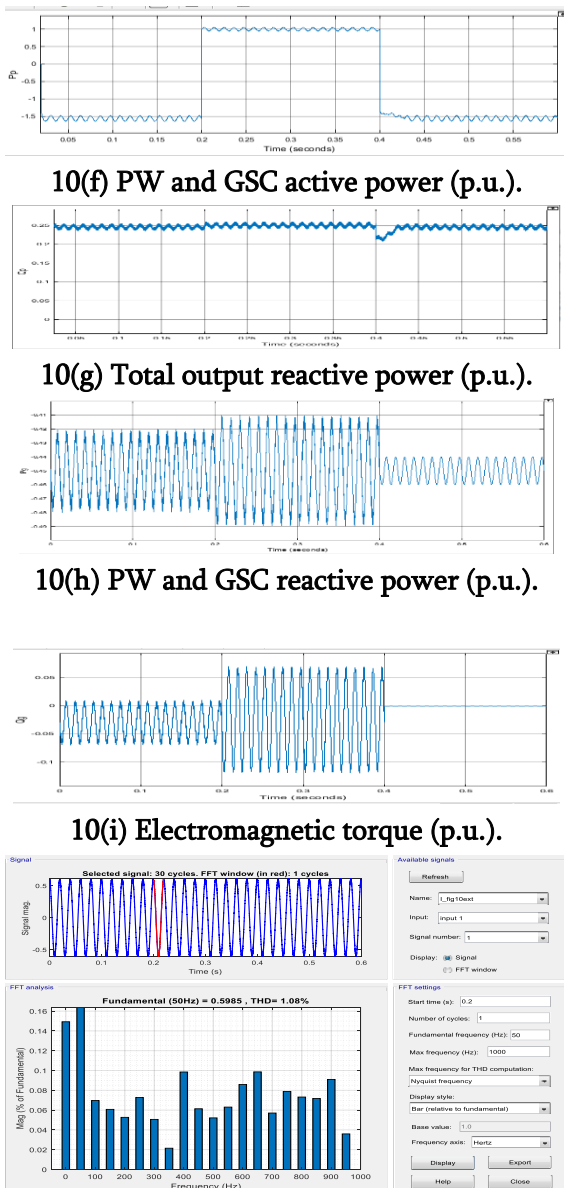
FIGURE 10. Waveforms with elimination of torque oscillations and three selectable control objectives under 10% grid voltage unbalance (! r D 0:7 p.u., "D 10%).

Waveforms with a constant rotor rotational speed of 0.7 p.u. and a 10% grid voltage imbalance are shown in Fig. 10. The MSC is controlled to minimise torque oscillations while the GSC is controlled with three independently adjustable control targets. The reference values for the PW average active and reactive power are 1.0 p.u. and 0.2 p.u., respectively. The GSC's control objective is initially set to Objective I, and then at 0.2 and 0.4 seconds, it changes to Objective II and Objective III, respectively. Total output current imbalance is eliminated during

0-0.2 s, as indicated in Fig. 9&10 (a). Additionally, the negative sequence components of the GSC and PW currents satisfy with, as seen in Figures 9&10 (b) and 9&10 (c) (40). In Fig. 9&10, the oscillations of total output active power disappear right away when Objective II is applied at 0.2 s. (e). Additionally, Fig. 9&10 (f) demonstrates that throughout the period of 0.2–0.4 s, the oscillations of Pg are the opposite of those of Pp. This eliminates the oscillations of total output active power shown in Fig. 9&10 (e). Similar to this, when Objective III is chosen at 0.4 s, the oscillations of total output reactive power decrease, as is shown in Fig. 9&10. (g). There are no oscillations in the total output reactive power, as illustrated in Fig. 9&10 (h), where Qg and QP oscillations are both zero. The electromagnetic torque oscillations and PW reactive power oscillations are eliminated throughout the entire process, as demonstrated in Fig. 9&10 (i) and Fig. 9&10 (h). Moreover, as shown in Fig. 9&10 (j), the DC link voltage contains 5% (3% during 0.2-0.4 s) oscillations at 100 Hz, which is caused by the fact that the active power of MSC (CW) contains oscillations at 100 Hz. Thus, it is clear from Fig. 9&10 that the proposed control objectives, which include eliminating torque oscillations and three selectable control objectives, namely, eliminating unbalanced total output current, oscillations of the total output active, and oscillations of the total output reactive power, have each been fully achieved. In addition, as can be observed from Fig. 9&10 (b), Fig. 9&10 (c), Fig. 9&10 (d), Fig. 9&10 (f) and Fig. 9&10(h), the GSC currents, average PW active and reactive power tracks their respective references extremely well and has better dynamic response.
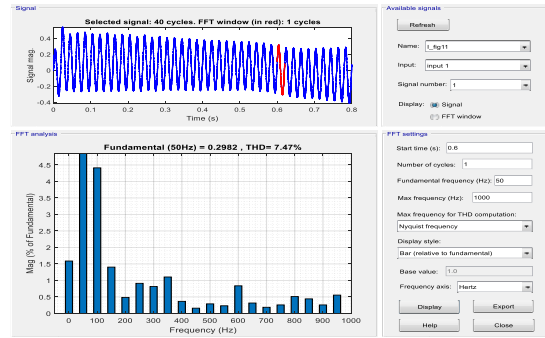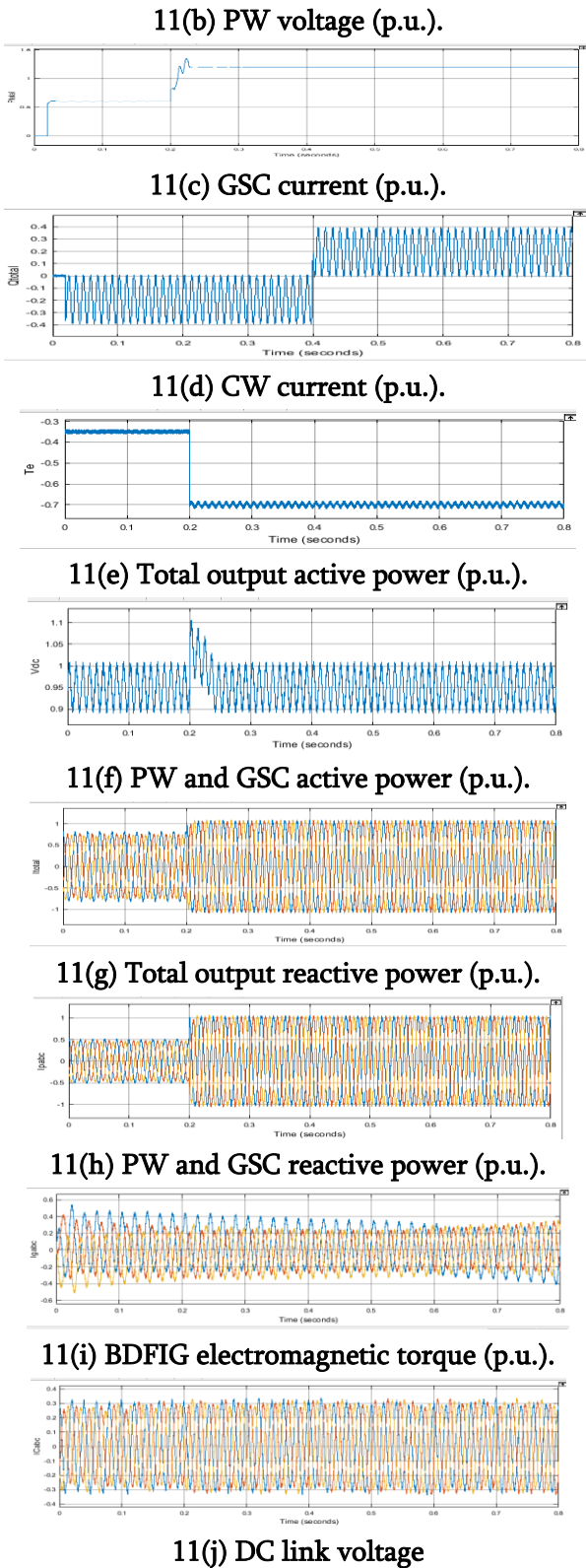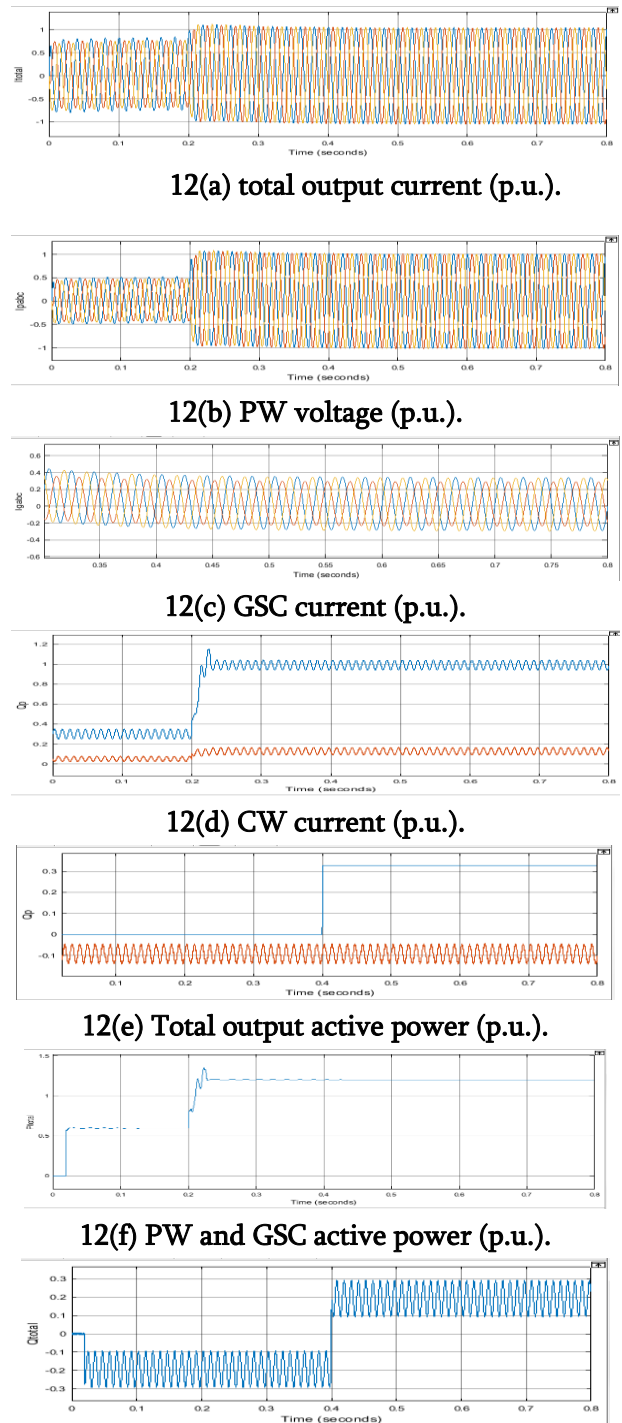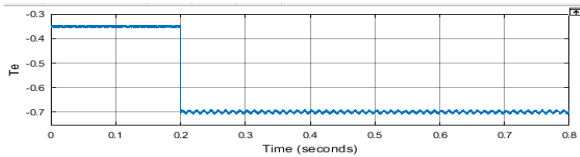

11(A) total output current (p.u.).

11(b) PW voltage (p.u.).

11(c) GSC current (p.u.).

11(d) CW current (p.u.).

11(e) Total output active power (p.u.).

11(f) PW and GSC active power (p.u.).

11(g) Total output reactive power (p.u.).

11(h) PW and GSC reactive power (p.u.).
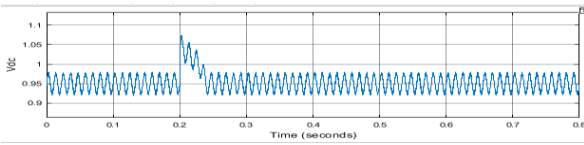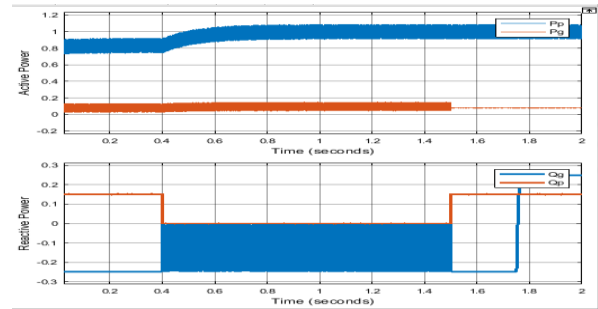
11(i) BDFIG electromagnetic torque (p.u.).

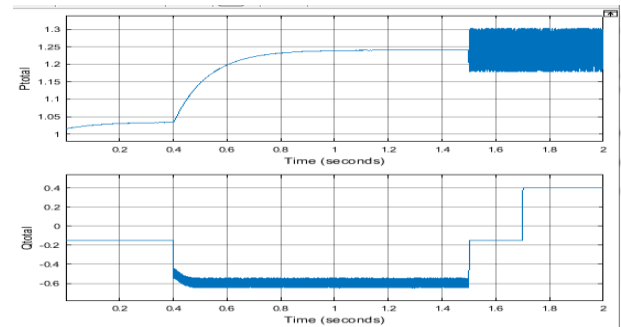11(j) DC link voltage

FIGURE 11. Waveforms with two control modes under ε = 10% grid voltage unbalance (ωr = 1.2 p.u.).

12(a) total output current (p.u.).

12(b) PW voltage (p.u.).

12(c) GSC current (p.u.).

12(d) CW current (p.u.).

12(e) Total output active power (p.u.).

12(f) PW and GSC active power (p.u.).

12(g) Total output reactive power (p.u.).

12(h) PW and GSC reactive power (p.u.).

12(I) BDFIG electromagnetic torque (p.u.).
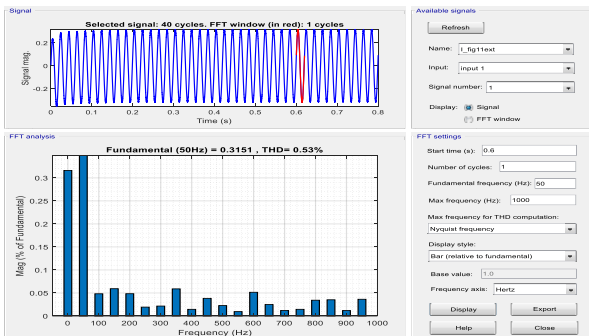
12(j) DC link voltage (p.u.). (B) Control mode 2.

FIGURE 12. Waveforms with two control modes under "D 10% grid voltage unbalance (! R D 1:2 p.u.).

The system reactions in Control mode 1 are shown in Fig. 11&12a. Torque and PW reactive power oscillations are eliminated, as demonstrated in Fig. 11&12a A (h) and Fig. 11&12a A I PW current unbalance is only 1%, which is extremely low. This is due to the intended MSC control using Control mode 1. However, due to limited control over the positive and negative sequence of the GSC's current under unbalanced grid voltage, as depicted in Fig. Figures 11&12a A(a), 111&12a A(c), 11&12a A(e), and Figure 11&12a A (f) Figures 11&12a A(g) and 11&12a A (j), A very large 100Hz oscillation of the total output active power (12.5%, 0-0.2 s; 25%, 0.2-0.8 s), reactive power (10%, 0-0.8 s), and DC link voltage (3%, 0-0.2 s; 5% to 6%, 0.2-0.8 s) is caused by the GSC's current, which is also severely distorted. The system reactions in Control mode 2 are shown in Fig. 11B. As predicted, the proposed control eliminates all oscillations in the electromagnetic torque, PW reactive power, and total output active power, as shown in Fig.11B (e), (h), and I respectively. Additionally, as seen in Figs. 11B(f) and

11B(h), the control for the average PW active power and reactive power is decoupled, and the average PW active and reactive power closely follows the values of the corresponding references. Thus, it can be concluded from Fig. 11 that the suggested control has great dynamic and steady control performance, can implement decoupling control, and can exactly achieve control targets.
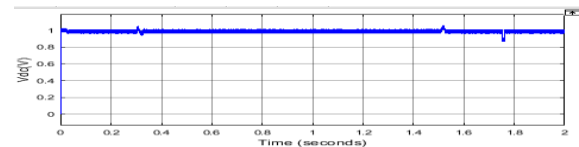

13(a) total output current (p.u.). (b) CW current (p.u.). (c) Total output active power (p.u.). (d) PW and GSC active power (p.u.)

13(e) Total output reactive power (p.u.). (f) PW and GSC reactive power (p.u.)
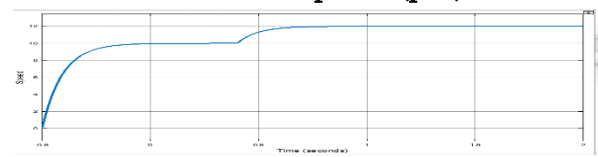
13(g) Mechanical torque and electromagnetic torque (p.u.)

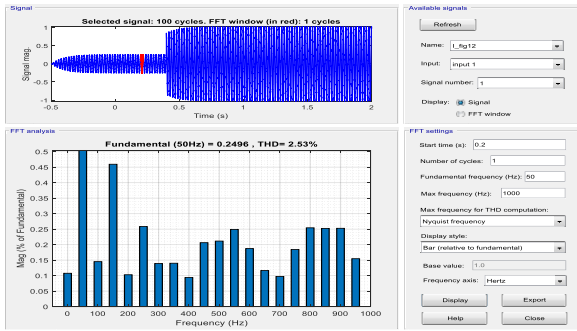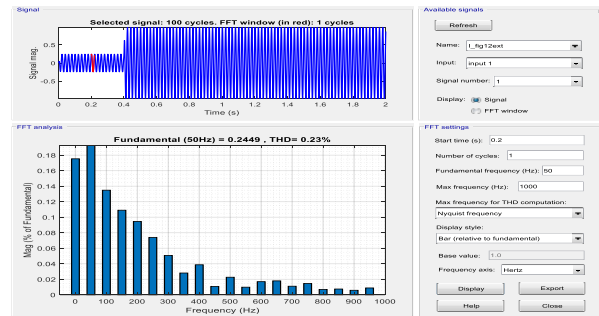13 (h) Rotor rotating speed (p.u.). (i) DC link voltage (p.u.).

FIGURE 13. Waveforms with variation of rotating speed under "D 10% grid voltage unbalance.

14(a) total output current (p.u.).

14(b) CW current (p.u.).

14(c) total output active power (p.u.).

14(d) PW and GSC active power (p.u.) (e) Total output reactive power (p.u.).

14(f) PW and GSC reactive power (p.u.). (g) Mechanical torque and electromagnetic torque (p.u.).

14 (h) Rotor rotating speed (p.u.). (i) DC link voltage (p.u.).

FIGURE 14. Waveforms with variation of rotating speed under "D 10% grid voltage unbalance.
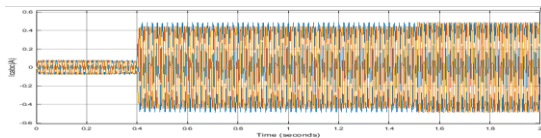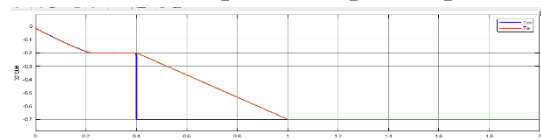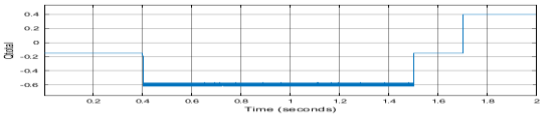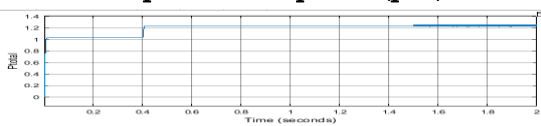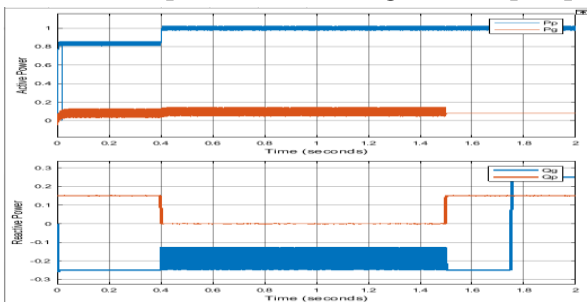
Figure 13&14 displays the outcomes. Figures 13&14(c), 13&14 (d), 13&14 (g), and 13&14 (h) show that three selectable control objectives—eliminating unbalanced total output current, oscillations of the total output active and reactive power, and the elimination of torque oscillations—have been precisely attained during intervals of 0.3 seconds, 1.5 seconds, 2 seconds, and 0 seconds, respectively. Additionally, in accordance with Fig. 12(d) and Fig. Decoupling control and the superior control performance for the average PW active power and reactive power have been confirmed once again in Fig. 13&14(g) and. As a result, the suggested control mechanism continues to operate satisfactorily despite fluctuations in torque and rotor speed.

V. CONCLUSION

In this paper, the simulation model of a DFIG-based wind turbine system under grid voltage unbalance is implemented in detail. Based on the proposed DFIG-WECS, a MPC controller strategy is employed for 5-level CHB-based MSC and GSC. Compared to conventional controllers, the proposed MPC control for GCS and MSC is more accurate. In this proposed system, GSC is employed for coordinated control with MSC to eliminate unbalanced total output current and oscillations of the total output active and reactive power. The effectiveness of the proposed MPC control is verified by means of simulation analysis and case studies. The results demonstrated that the

proposed MPC control can improve the capability of withstanding grid voltage unbalance significantly and provide excellent dynamic and stable performance.

VI. REFERENCES

[1]. Tsili, M.; Papathanassiou, S. A review of grid code technical requirements for wind farms. IET Renew. Power Gen. 2009, 3, 308–332.

[2]. Erlich, I.; Winter, W.; Dittrich, A. Advanced Grid Requirements for the Integration of Wind Turbines into the German Transmission System. In Proceedings of IEEE Power Engineering Society General Meeting 2006, Montreal, Quebec, Canada, 18–22 June 2006.

[3]. Federal Energy Regulatory Commission. Regulatory Order No. 661-A: Interconnection for Wind Energy. Available online: http://www.ferc.gov/industries/electric/indus-act/gi/wind.asp (accessed on 21 February 2013).

[4]. Thomas, A. Wind Power in Power Systems; Wiley: New York, NY, USA, 2005.

[5]. Mohseni, M.; Islam, S.; Masoum, M. Impacts of symmetrical and asymmetrical voltage sags on DFIG-based wind turbines considering phase angle jump, voltage recovery, and sag parameters. IEEE Trans. Power Electron. 2011, 26, 1587–1598.

[6]. Yang, L.; Xu, Z.; Ostergaard, J.; Dong, Z.; Wong, K. Advanced control strategy of DFIG wind turbines for power system fault ride through. IEEE Trans. Power Syst. 2012, 27, 713–722.

[7]. Zhang, W.; Zhou, P.; He, Y. Analysis of the By-Pass Resistance of an Active Crowbar for Doubly-Fed Induction Generator Based Wind Turbines under Grid Faults. In Proceedings of International Conference on Electrical Machines and Systems (ICEMS 2008), Wuhan, China, 17–20 October 2008.

[8]. Pannell, G.; Atkinson, D.; Zahawi, B. Minimum-threshold crowbar for a fault-ride-through grid-code-compliant DFIG wind turbine. IEEE Trans. Energy Convers. 2010, 25,750–759.

[9]. Morren, J.; de Haan, S. Ride through of wind turbines with doubly fed induction generator during a voltage dip. IEEE Trans. Energy Convers. 2005, 20, 35–441.

[10]. Yang, J.; Fletcher, J.; O'Reilly, J. A series-dynamic-resistor-based converter protection scheme for doubly-fed induction generator during various fault conditions. IEEE Trans. Energy Convers. 2010, 25, 422–432.

[11]. Causebrook, A.; Atkinson, D.; Jack, A. Fault ride-through of large wind farms using series dynamic braking resistors. IEEE Trans. Power Syst. 2007, 22, 966–975.

[12]. Flannery, P.; Venkataramanan, G. Unbalanced voltage sag ride through of a doubly fed induction generator wind turbine with series grid-side converter. IEEE Trans. Ind. Appl. 2009, 45, 1879–1887.

[13]. Wessels, C.; Gebhardt, F.; Fuchs, F.W. Fault ride-through of a DFIG wind turbine using a dynamic voltage restorer during symmetrical and asymmetrical grid faults. IEEE Trans. Power Electron. 2011, 26, 807–815.

[14]. Guo, W.; Xiao, L.; Dai, S. Enhancing low-voltage ride-through capability and smoothing output power of DFIG with a superconducting fault-current limiter–magnetic energy storage system. IEEE Trans. Energy Convers. 2012, 27, 277–295.